

Computing foaming flows across scales: from breaking waves to microfluidics

Petr Karnakov^a, Sergey Litvinov^a, and Petros Koumoutsakos^{a,b,*}

^aComputational Science and Engineering Laboratory, ETH Zurich, Switzerland

^bSchool of Engineering and Applied Sciences, Harvard University, Cambridge, MA 02138, USA

*corresponding author: petros@seas.harvard.edu

March 3, 2021

Abstract

Crashing ocean waves, cappuccino froths and microfluidic bubble crystals are examples of foamy flows. Foamy flows are critical in numerous natural and industrial processes and remain notoriously difficult to compute as they involve coupled, multiscale physical processes. Computations need to resolve the interactions of the bubbles with the fluid and complex boundaries, while capturing the drainage and rupture of the microscopic liquid films at their interface. We present a novel multilayer simulation framework (Multi-VOF) that advances the state of the art in simulation capabilities of foamy flows. The framework introduces a novel scheme for the distinct handling of multiple neighboring bubbles and a new regularization method that produces sharp interfaces and removes spurious fragments. Multi-VOF is verified and validated with experimental results and complemented with open source, efficient scalable software. We demonstrate capturing of bubble crystalline structures in realistic microfluidics devices and foamy flows involving tens of thousands of bubbles in a waterfall. The present multilayer framework extends the classical volume-of-fluid methodology and allows for unprecedented large scale, predictive simulations of flows with multiple interfaces.

Main

Bubbly foams are the signature of violent crashes of ocean waves and happy times accompanied by champagne. Bubble coalescence and collapse is central to new products and technologies in areas ranging from food, to cosmetics and drug delivery through precision microfluidics for emulsions and foams [34, 1, 28]. Drainage and rupture of the liquid film separating bubbles leads to their coalescence. Surfactants [16] and other impurities, such as electrolytes [13], in the liquid can delay or prevent coalescence. Bubbles in clean liquids can also collide without coalescence if the film drainage time is sufficiently large [9]. Foams are composed by many bubbles separated by stable liquid films. Foams are structural elements of insect, fish and frog nests and central to numerous industrial processes and medicine [35, 21, 17].

The simulation of foamy flows, involving non-coalescing bubbles, presents a number of formidable challenges in addition to those associated with resolving the bubble interactions with the fluid flow and the solid boundaries [36]. In foams the thickness of the film is usually several orders of magnitude smaller than the size of bubbles. In the limit of zero film thickness, the evolution of (dry) foams can be predicted using Lagrangian techniques that track the surfaces between bubbles with multiple junctions [7]. State of the art techniques involve Eulerian methods such as the Voronoi Implicit Interface Method (VIIM) [32] that uses a single level-set function for all interfaces. More recently, methods such as the Lattice Boltzmann [27] have captured the effect of thin films using an empirical collision potential but resort to mesoscale models with limited density ratio and artificial compressibility. In simulations of bubble collisions in turbulent flows [18], a short range repulsive force between bubbles has been used to increase the surface tension near the contact. However, this can only remedy rapid collisions but not account for stable multi-bubble structures with thin films as in foams.

The classical volume-of-fluid (VOF) methodology [22, 29] has found widespread success in simulations of engineering flows involving interfaces. However, VOF leads to spurious coalescence of bubbles that approach each other at a distance below one computational cell. Such spurious coalescence can be prevented by introducing distinct volume fraction fields for each bubble in the multi-marker volume-of-fluid [4] or distinct functions in level-set methods [12]. This prevention of coalescence has a computational cost that is proportional to the number of bubbles in the simulation (i.e. $\mathcal{O}(N_{\text{bubbles}} N_{\text{cells}})$), and it is prohibitive for systems with a few hundred bubbles even in today's computer architectures. Furthermore as each distinct volume fraction field corresponds to only one bubble keeping track of all volume fraction fields is redundant. We propose a method to store

arXiv:2103.01513v1 [physics.comp-ph] 2 Mar 2021

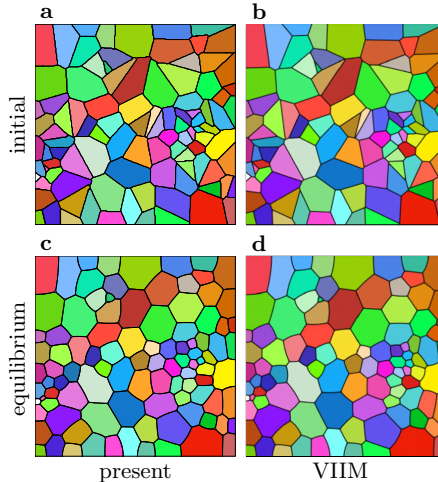


Figure 1: Constrained mean curvature flow. The initial field (a,b) is a Voronoi diagram. Multi-VOF method (c) produces results similar to that of the Voronoi implicit interface method (VIIM) [32] (d) on the same mesh of 256^2 cells. Interfaces at triple junctions form 120° angles.

multiple fields in a compact way so that the number of the necessary scalar fields is constant, independent on the number of bubbles in the simulation (see Methods). This technique is combined with VOF to simulate flows with non-coalescing bubbles. The proposed multilayer volume-of-fluid method (Multi-VOF) overcomes the above mentioned challenges and allows for predictive simulations of flows involving thousands of interacting and non-coalescing bubbles. Multi-VOF requires only a fixed number of fields, and its computational cost is independent on the number of bubbles in the simulation.

Results

Constrained mean curvature flow, comparison with VIIM

The capabilities of Multi-VOF are first assessed in the limiting case of fluid flows with surface tension but no inertia. In this case the governing equations (see Methods) simplify to a single equation for the velocity field $\mathbf{u} = \kappa \nabla \alpha - \nabla p$, where the scalar field $p(\mathbf{x}, t)$ is used to ensure that the velocity field is divergence-free ($\nabla \cdot \mathbf{u} = 0$). We use this velocity field with the advection equation to compare Multi-VOF with the pioneering work in [32]. The initial conditions are adopted from [32] and represent a Voronoi diagram of a randomly chosen set of 100 points with homogeneous Neumann boundary conditions for the volume fraction fields. Initially, the interfaces are straight lines and form multiple junctions at arbitrary angles. As time evolves, only triple junctions remain and the angles between the lines approach 120° . In Fig. 1, we compare the solution by our method and the Voronoi Implicit Interface Method [32]. For Multi-VOF, dry foams are a limiting case since there is no special treatment of triple junctions leading to the formation of small voids near the junctions. Nevertheless, the results of Multi-VOF and VIIM are in excellent agreement for the same mesh size. Applying penalization techniques can further improve the results by removing the voids.

Microfluidic crystals

Bubbles and droplets in microfluidic devices organize into lattices called microfluidic crystals [5]. They serve as prototypes of foam structures, compartments for chemical reactions, and parts in production of metamaterials [25]. A recent study [27] applied a mesoscale lattice Boltzmann (LB) model to capture these flow structures. The LB model includes a short range forcing term that describes the combined effect of surface tension and near-contact interactions to prevent coalescence. The authors compare their results with experimental data [25] on foams of air bubbles in water. However, due to the limited density ratio of the LB approach, their mesoscale model is instead tuned for water drops embedded in oil.

Using the Multi-VOF method, we aim to reproduce the experimental study [31] on the formation of microfluidic crystals of bubbles in water. Limited by numerical stability and computational cost, we use lower values of the density ratio, surface tension, viscosity and the channel length. The device is based on a flow-focusing geometry [20] and consists in a planar network of rectangular ducts of height H with three inlets. The gas is injected from one inlet at a fixed pressure P_g relative to the outlet pressure, and the liquid comes through the other two with a total flow rate Q_l . The gas enters the channel through a contracting duct that ends with

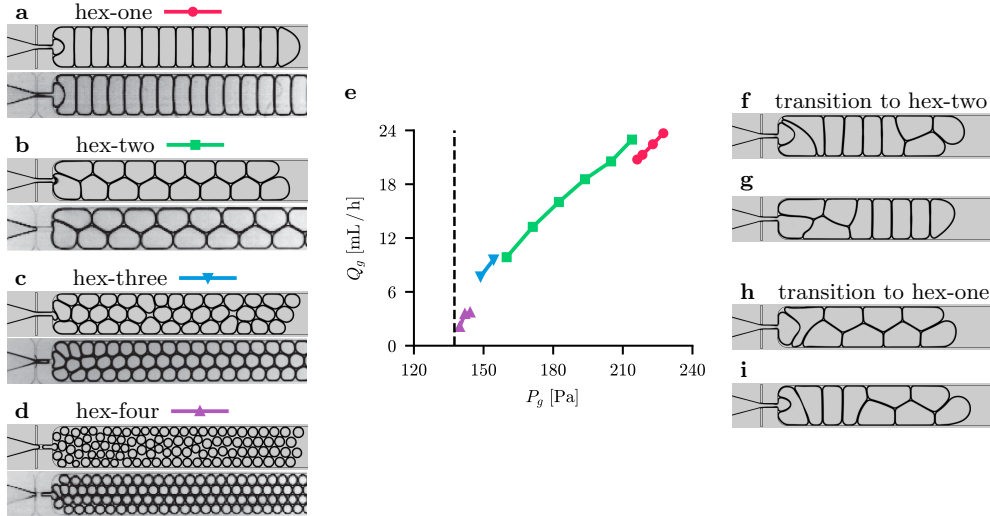


Figure 2: (a-d) Crystalline structures of bubbles from simulations compared to experimental images [31]. Hex-one ($P_g = 216$ Pa, a), hex-two ($P_g = 194$ Pa, b), hex-three ($P_g = 149$ Pa, c), and hex-four ($P_g = 140$ Pa, d). (e) Gas flow rate as a function of the inlet gas pressure. The flow starts once the pressure exceeds the capillary threshold ---. Lines correspond to hex-one ●, hex-two ■, hex-three ▲, and hex-four ▲ structures. (f-g) Spontaneous transitions between hex-one and hex-two with $L = 5.3$ mm and $P_g = 225$ Pa. Snapshots are taken at times 443 ms (f), 460 ms (g), 512 ms (h), and 529 ms (i).

an orifice of a width W_0 expanding into the collection channel. Walls of the channel are no-slip boundaries. Parameters of the simulation are given in Supplementary Table 1.

Bubbles in such devices are generated by the breakup of the air thread in the inlet channel. The period of breakup is determined by the liquid flow rate and not by capillary time scales despite an apparent similarity to the Rayleigh-Plateau instability [20]. In simulations, we forcibly separate the air thread at a regular interval T_b . Unless stated otherwise, the period of breakup equals $T_b = 0.5 W_0^2 H / Q_l$ estimating the time it takes for the liquid to fill the volume of a cavity forming right before the breakup.

To obtain various crystalline structures, we vary the inlet gas pressure P_g . The gas flow rate Q_g and the bubble volume V_b as functions of pressure are plotted in Fig. 2. The gas flow starts as soon as the pressure exceeds the capillary threshold estimated as $P_{\text{cap}} = \sigma(\frac{1}{H} + \frac{1}{W_0})$. Raising the pressure enhances the gas flow rate Q_g and, since the breakup period T_b is kept constant, increases the size of bubbles. Each simulation with a given P_g is advanced until equilibration, the evolution of the gas flow rate for selected values of P_g is shown in Supplementary Figure 9. Closely packed bubbles form 120° angles at triple junctions, and junctions at the walls are 90° . Depending on the size, the bubbles organize into regular structures, or flowing crystals. The structures are named by the number of bubbles that fit in the channel width [31]: hex-one, hex-two, hex-three and so on. Examples of the structures together with experimental images are shown in Fig. 2 and Movies S1-S4. Stability of each structure is dictated by the corresponding value of the surface energy. Smaller bubbles transition to higher-order structures.

The dissipation in foam is proportional to its *wetting perimeter*, i.e. the length of the menisci that confine the liquid between the interface and the channel walls [8]. Hex-one bubbles dissipate more than hex-two bubbles and correspond to a slower flow [31]. Our simulations capture this effect as seen from Fig. 2 and Movie S5. If the structure remains the same, increasing the pressure leads to a faster flow. Conversely, if the structure changes, increasing the pressure may decrease the flow rate. For example, increasing P_g from 205 Pa to 216 Pa reduces the flow rate as the flow transitions from hex-two to hex-one.

One behavior observed near such transitions is a bubbling oscillator [30]. It is based on the interplay between the stability and dissipation of hex-one and hex-two structures. As the channel fills with hex-one bubbles, the flow rate decreases due to growing dissipation. The bubbles entering the channel become smaller such that the hex-one structure is no longer stable. The flow transitions to hex-two and accelerates again. The process repeats indefinitely. In our simulations, we obtain such an oscillator with $L = 5.3$ mm, $T_b = 0.46 W_0^2 H / Q_l$ and the inlet pressure $P_g = 225$ Pa. The flow rate plotted in Supplementary Figure 9 oscillates in time. Examples of the transitions between hex-one and hex-two are shown in Fig. 2.

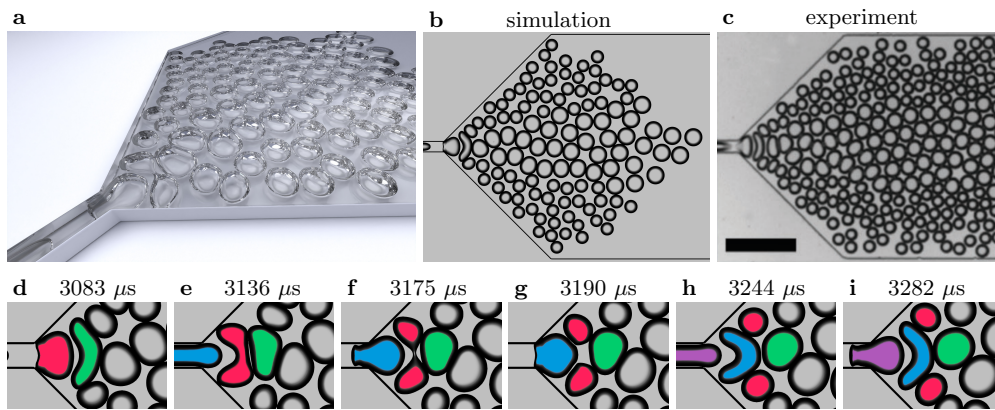


Figure 3: (a) Overall view of the microfluidic device for generation of bidisperse foams at $t = 8749 \mu\text{s}$. (b) Snapshot from the simulation at $t = 8872 \mu\text{s}$. (c) Experimental image [37]. The scale bar is $500 \mu\text{m}$. (d-i) Alternation between bubble-bubble pinch-off and elongation without breakup. snapshots at $t = 3083, 3136, 3175, 3190, 3244,$ and $3282 \mu\text{s}$ respectively. Colors highlight the same bubbles in all snapshots. Split bubble (red), wall bubble (green), and intact bubble (blue).

Bidisperse foam generation

A recently demonstrated microfluidic device [37] makes use of bubble-bubble pinch-off to generate bidisperse foams. Here we reproduce its operation numerically. The device represents a planar network $60 \mu\text{m}$ high where a narrow channel expands with 45° walls to a collection channel. Bubbles are generated periodically at an interval of $111 \mu\text{s}$ to maintain the volume fraction of gas at 0.645. At each cycle, the bubble is inserted in the narrow channel by replacing the liquid with gas in a part of the channel. Parameters of the simulation are summarized in Supplementary Table 2. Walls of the channel are no-slip boundaries.

The overall view of the device is shown in Fig. 3a and Movie S6. The snapshot from the simulation in Fig. 3b compared to the experimental image [37] (Fig. 3d therein) indicates a good agreement with the experimental data since both have similar shapes and positions of the split and intact bubbles.

Bubbles entering the expansion alternate between two types of behavior illustrated in Fig. 3d-i. They either split into smaller bubbles or remain intact. For example, one bubble (Fig. 3d) enters the expansion, elongates under the shear stress (Fig. 3e) from the liquid flow and splits into two daughter bubbles (Fig. 3f). The *wall bubble* confines the liquid flow. The two daughter bubbles then migrate sideways, leaving a gap of liquid between the wall bubble (Fig. 3g) and the next incoming bubble, which only elongates without breakup and eventually restores its shape. Alternation of these two regimes drives the generation of bidisperse foams.

Another part of the pinch-off process is the *pincher bubble* upstream of the split bubble (blue in Fig. 3e and purple in Fig. 3h). One question arising here is whether the pincher bubble actually causes the breakup. The explanation given in the experimental study [37] suggests that the pincher bubble increases the flow confinement and the corresponding shear stresses on the split bubble, leading to breakup. To verify this, we compare two simulations: one with a normal pinch-off event and one where the pincher bubble is delayed by $60 \mu\text{s}$. Both simulations were done with the length of the collection channel set to $L = 0 \mu\text{m}$ to reduce the computational cost, still leaving a sufficient separation from the outlet. Fig. 4 shows that the pincher bubble does not trigger the pinch-off event. Delaying the pincher bubble does not change the flow of the liquid near the split bubble (Fig. 4h and Fig. 4k). This indicates that the pinch-off is triggered by the wall bubble downstream rather than the pincher bubble upstream.

Clustering of bubbles

Clustering of bubbles floating on the surface of water is an example of self-assembly known as the Cheerios effect [38], named after the observation that breakfast cereals floating in milk often clamp together. A bubble floating on the surface creates an elevation attracting other bubbles due to buoyancy. Many floating bubbles are hence attracted to each other and form clusters.

Fig. 5 shows clusters of bubbles obtained numerically and experimentally. In the experimental setup, a large tank is filled halfway with tap water and a common detergent. One end of a tube with an inner diameter of about 0.3 mm is submerged into water, and the other end is connected to a syringe filled with air. The plunger is then abruptly pushed until bubbles start to appear. This generates bubbles of about 2 mm in diameter. To visualize the deformation of the surface, the bottom of the tank is covered with a patterned sheet. In the simulation, spherical bubbles are generated at the bottom at regular intervals. Parameters are in Supplementary

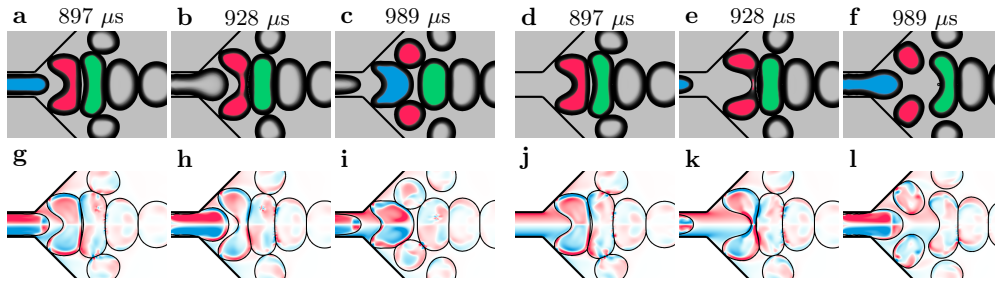


Figure 4: Effect of delaying the pincher bubble. Standard case (a-c, g-i) and case with delayed pincher bubble (d-f, j-l) at various time instances. (a-f) Bubble surfaces with the highlighted pincher bubble (blue), split bubble (red) and wall bubble (green). (g-l) Component of vorticity normal to the view plane (red for counterclockwise and blue for clockwise). Delaying the pincher bubble does not prevent breakup.

Table 3. Both in the experiment and the simulation, bubbles floating on the surface form clusters and organize in a hexagonal lattice. Movie S7 shows the simulation results.

Foaming waterfall

Natural surfactants in sea water can suppress coalescence as well. Oceans are covered with foam generated by breaking waves. The following application is an example of such flows in the limiting case without coalescence. A rectangular tank 100 mm high is filled halfway with water. A waterfall enters the tank at a given velocity. Supplementary Table 4 lists the simulation parameters. Results of the simulation are in Fig. 6 with additional snapshots in Supplementary Figure 12 and Movie S8. On the finest mesh consisting of $768 \times 384 \times 384$ cells, the simulation took 20 hours on 1152 compute nodes of the Piz Daint supercomputer equipped with 12-core CPU Intel Xeon E5-2690 v3 processors. Two major mechanisms of air entrainment [24] are observed in this simulation: entrapment of a tube of air when the sheet of water impacts the surface and entrainment around the impact site as the waterfall drags air into the water. The entrained bubbles rise to the surface and create a layer of foam. As seen from the horizontal cross-section of the foam in Fig. 6, the bubbles are separated by thin membranes (lamellae) that form multiple junctions (Plateau borders) at angles approaching 120° .

The distribution of the bubble size in Fig. 6 matches a scaling law [19] $N(r) \propto r^{-10/3}$, where $N(r)$ is the number of bubbles of radii in the range $r \pm 0.1$ mm. The model stems from the assumption that the inflow of air per unit volume is constant, and the number of bubbles depends only on the turbulent dissipation rate and the bubble radius. This scaling law is commonly observed for bubbles generated by breaking waves and has been reported in experimental [14] and numerical [15] studies.

Discussion

The multilayer volume-of-fluid method can simulate flows with many bubbles and drops that do not coalesce. It represents many bubbles with a fixed number of volume fraction fields and assigns colors to bubbles to distinguish them. An additional technique of interface regularization based on forward-backward advection improves the accuracy of the advection scheme. The presented applications show that the method can reproduce experiments on generation of foam in microfluidic devices and clustering of bubbles floating in water.

The proposed methodology advances the state of the art in simulations of flows with multiple interfaces in the following categories:

1. Efficiency: The method uses a fixed number of volume fraction fields on an Eulerian mesh. The computational complexity of the advection algorithm is linear with the number of cells and does not depend on the number of bubbles.
2. Compatibility with existing methods: The method is compatible with existing stencil-based methods for interface capturing and curvature estimation, including the popular volume-of-fluid and level-set methods. For dry foams, the method can recover the results of VIIM at comparable resolutions.
3. Capturing topology changes and multiple bubble junctions: Breakup and coalescence of bubbles including thin liquid films and triple lines are captured without employing ad-hoc parameters.
4. Coupling with models of film drainage and rupture: Coalescence can be controlled by assigning appropriate color functions to interacting bubbles.

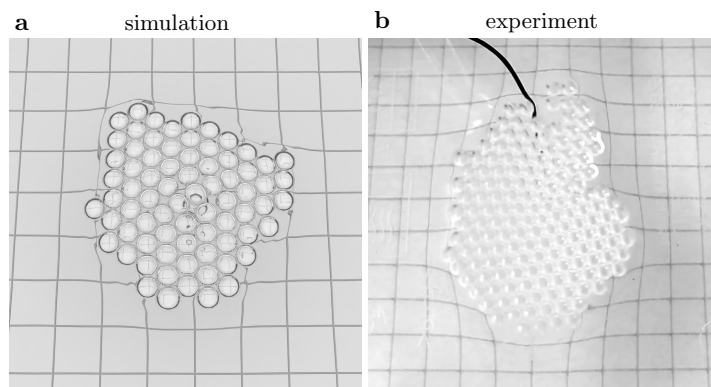


Figure 5: Clustering of bubbles floating on water. (a) Simulation using the Multi-VOF method (b) Experiment in soapy water. The size of square cells is 4 mm.

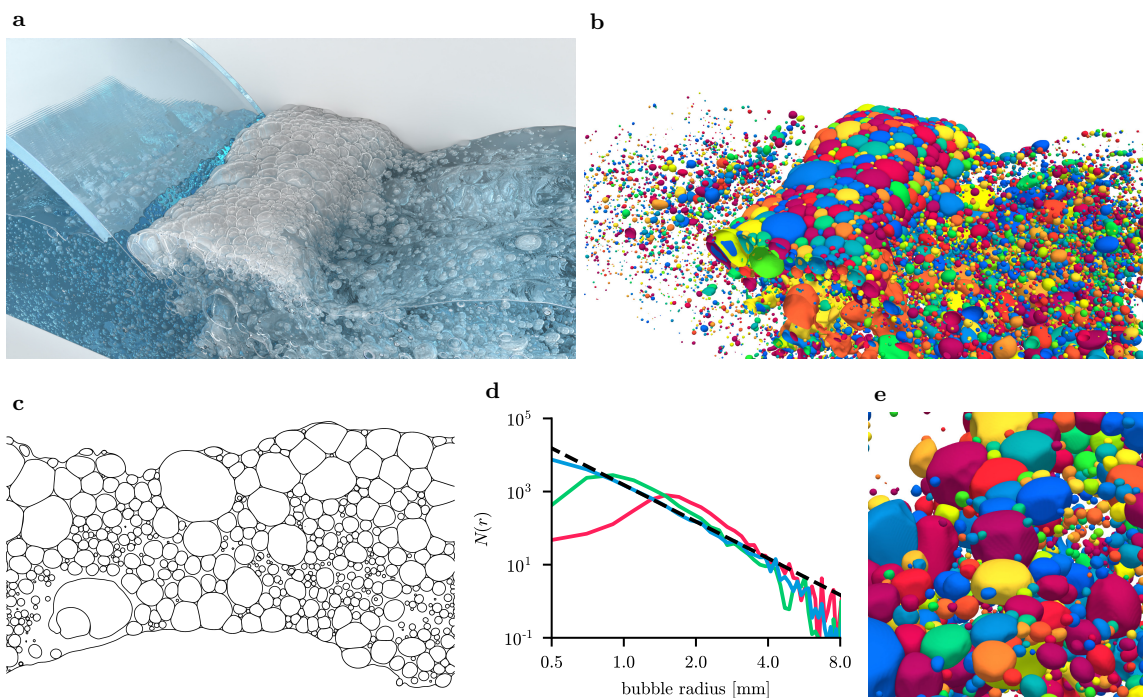


Figure 6: Foaming waterfall. (a) Overall view of the interface at $t = 1.2$ s. (b) Same view showing bubbles under the surface with arbitrary colors. (c) Horizontal cross-section of the interface at $t = 1.2$ s. Clusters of bubbles on the surface show characteristic features of foam: bubbles are separated by thin membranes (lamellae) with multiple junctions (Plateau borders). (d) Histogram of the bubble radius. $N(r)$ is the number of bubbles with the equivalent radius in the range $r \pm 0.1$ mm. Results for different mesh sizes of 96 (red), 192 (green), and 384 (blue) cells in the height compared to scaling law [19] $N(r) \propto r^{-10/3}$ (black dashed). The values are averaged in time over $1 < t < 1.2$ s. (e) Close-up of (b) with half of the bubbles removed.

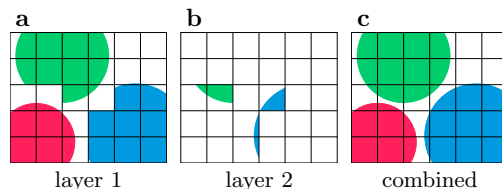


Figure 7: Two-layer volume fraction field representing three bubbles. Individual layers (a,b) contain at most one bubble per cell, while the combined field (c) describes overlapping interfaces.

5. High performance implementation: The method only involves stencil operations and is readily integrated in high performance software for structured grids.

We believe that Multi-VOF opens new horizons for simulating a wide variety of flows from the micro to the macroscale, including wet foams, turbulent flows with bubbles, suspensions and emulsions in microfluidics. Moreover, the efficiency of the code allows for extensive studies in control and optimization of bubbly flows.

Limitations

The method describes the complete prevention of coalescence and an empirical criterion is used in cases where the residence time of bubbles is finite. Since bubbles are distinguished as connected components of the volume fraction field, the method does not prevent coalescence if a deformed bubble folds back onto itself. Two small bubbles can penetrate each other and form concentric configurations when their radius is comparable to one computational cell. The method can be improved by adopting a semi-implicit discretization of the surface tension force [11].

Generation of bubbles requires additional modeling. In simulations, we forcibly separate the air thread at regular intervals. Otherwise, the gas thread remains continuous unless the inlet pressure is sufficiently low. Such continuous regimes are observed experimentally under certain conditions [2] but not in the experimental study of interest [31]. One explanation for this discrepancy is the effect of wetting [2] that may narrow the gap between the liquid-gas interface and the channel walls since the static contact angle of polydimethylsiloxane (PDMS) is 104° [26] while our model assumes 180° . Another possibility is that the viscous flow of the liquid upstream of the orifice is not sufficiently resolved in the simulations.

Methods

Multilayer fields

Consider a discrete domain Ω consisting of cells $c \in \Omega$, where the number of cells is $|\Omega| = N_{\text{cells}}$. A conventional cell field $\phi: c \mapsto \phi_c$ is a mapping from cell c to a value. A *cell-color* field $\hat{\phi}: (c, q) \mapsto \hat{\phi}_c(q)$ is a mapping from cell c and *color* $q \in \mathbb{R}$ to a value. Overlapping bubbles can be represented by a single cell-color field if each bubble is assigned a unique color. The restriction operation $\hat{\phi}|_q$ constructs a conventional field $\hat{\phi}|_q: c \mapsto \hat{\phi}_c(q)$ from a cell-color field $\hat{\phi}$ given a color q . Using this operation, any standard routine, such as computing the normals or solving the advection equation, can be applied to a cell-color field by individually selecting all possible colors. To store a cell-color field $\hat{\phi}$, we use a sequence of conventional fields for values and colors separately. Assume that any cell contains at most L bubbles and their shapes are represented by the cell-color volume fraction field $\hat{\alpha}$. The colors are stored in fields $q^l: c \mapsto q_c^l$, $l = 1, \dots, L$ defined in each cell c as

$$q_c^l = \begin{cases} q_l, & 1 \leq l \leq L', \\ q_{\text{none}}, & \text{otherwise,} \end{cases}$$

where $\{q_1, \dots, q_{L' \leq L}\}$ are all colors for which $\hat{\alpha}_c(q) > 0$ and q_{none} is a distinguished *none* color (e.g. $q_{\text{none}} := -1$). The corresponding values are stored in fields $\phi^l: c \mapsto \phi_c^l$, $l = 1, \dots, L$

$$\phi^l = \begin{cases} \hat{\phi}(q_c^l), & q_c^l \neq q_{\text{none}}, \\ \text{undefined}, & \text{otherwise.} \end{cases}$$

The pairs (ϕ^l, q^l) are referred to as *layers* and the sequences (ϕ^1, \dots, ϕ^L) and (q^1, \dots, q^L) constitute a *multilayer* field. The order in which the colors are stored is insignificant, i.e. all sequences (q_c^1, \dots, q_c^L) and $(\phi_c^1, \dots, \phi_c^L)$ are equivalent up to mutual permutation. Fig. 7 illustrates two layers that describe three overlapping bubbles.

Advection

By constructing conventional fields from a cell-color field, we can apply standard stencil-based algorithms to cell-color fields. One such algorithm, the PLIC (Piecewise Linear Interface Characterization) method [40] for advection, is described in the following. The PLIC method solves the advection equation given a velocity field \mathbf{u} $\frac{\partial \alpha}{\partial t} + (\mathbf{u} \cdot \nabla) \alpha = 0$. As the name stands, it performs a piecewise linear reconstruction by replacing the interface in each cell with a plane. Apart from the volume fraction field, it involves normals and plane constants. The normals $\mathbf{n} : \Omega \rightarrow \mathbb{R}^3$ are estimated from the volume fractions using the mixed Youngs-centered scheme [3] and the plane constants are computed from the normals and volume fractions using explicit formulas [33]. The fluid volume is reconstructed in each cell with a polyhedron formed by cutting the cell with the plane. The fluxes are then computed by advecting the polyhedrons according to the given velocity [3, 39]. The discretization uses directional splitting, and a step in one direction can be schematically written in terms of discrete operators \mathcal{N} and \mathcal{A} : $\mathbf{n}_c = \mathcal{N}(S^c[\alpha])$ and $\alpha_c^{\text{new}} = \mathcal{A}(S^c[\alpha], S^c[\mathbf{n}])$, where $S^c = (c_1, \dots, c_{27})$ is the sequence of cells in the $3 \times 3 \times 3$ stencil centered at c and $S^c[\phi] = (\phi_{c_1}, \dots, \phi_{c_{27}})$ are the corresponding values of a field ϕ . To apply this method to a cell-color field, the same procedure is repeated for all colors: $\hat{\mathbf{n}}_c(q) = \mathcal{N}(S^c[\hat{\alpha}|_q])$ and $\hat{\alpha}_c^{\text{new}}(q) = \mathcal{A}(S^c[\hat{\alpha}|_q], S^c[\hat{\mathbf{n}}|_q])$. In terms of multilayer fields q^l , α^l and \mathbf{n}^l , the normals are computed with the following algorithm

```

for  $c \in \Omega$ ,  $l = 1, \dots, L$  do
  if  $q_c^l \neq q_{\text{none}}$  then
    for  $i = 1, \dots, 27$  do
       $c' \leftarrow S_i^c$ 
       $\bar{\alpha}_i \leftarrow 0$ 
      for  $l' = 1, \dots, L$  do
        if  $q_{c'}^{l'} = q_c^l$  then
           $\bar{\alpha}_i \leftarrow \alpha_{c'}^{l'}$ 
        end if
      end for
    end for
     $\mathbf{n}_c^l \leftarrow \mathcal{N}(\bar{\alpha})$ 
  end if
end for

```

The total number of operations of this algorithm is $\mathcal{O}(L^2 N_{\text{cells}})$. Before proceeding with advection, the normals are corrected. When two or more interfaces enter one cell, we ensure that their normals are parallel. From the estimated normals $(\mathbf{n}_1, \dots, \mathbf{n}_{L'})$ we compute the average $\mathbf{n}_{\text{avg}} = \frac{1}{L'} \sum_{l=1}^{L'} \mathbf{n}_l \text{sign}(\mathbf{n}_l \cdot \mathbf{n}_1)$ and overwrite the normals as $\mathbf{n}_l \leftarrow \mathbf{n}_{\text{avg}} \text{sign}(\mathbf{n}_l \cdot \mathbf{n}_{\text{avg}})$. This correction prevents mutual penetration of interfaces.

The advection step is done similarly, but includes also new colors found in upwind cells. If the new volume fraction for an upwind cell color is positive, the color is added to the current cell. Colors corresponding to zero volume fractions are removed. For the number of layers we find sufficient $L = 4$ based on the case of close packing of rising bubbles in Supplementary Figure 7.

Connected-component labeling

Prevention of coalescence requires that all bubbles have unique colors. These unique colors can be assigned from initial conditions. For instance, using the indices of bubbles as colors. If the set of bubbles remains the same, the colors remain unique throughout the simulation. However, new colors are needed for injected bubbles or bubbles formed during breakups. To detect breakups and assign unique colors to all bubbles, we use connected-component labeling.

Starting with the old color fields q^l and volume fraction fields α^l , we construct new color fields \tilde{q}^l in which all bubbles have unique colors. Different bubbles are identified as connected components in the volume fraction field. Two neighboring cells and layers (c, l) and (c', l') are connected with an edge if they have positive volume fractions $\alpha_c^l > 0$ and $\alpha_{c'}^{l'} > 0$ and equal colors $q_c^l = q_{c'}^{l'}$.

To detect the connected components, we first initialize \tilde{q}_c^l with unique colors for all cells and layers. For instance, using an integer index enumerating all cells and layers (in total, $N_{\text{cells}} L$ colors). Then we iterate until convergence over all pairs of connected cells and layers choosing the minimal color. The procedure is implemented by the following algorithm


```

i ← 0
for c ∈ Ω , l = 1, ..., L do                                ▷ initialize with unique colors
     $\tilde{q}_c^l \leftarrow i$ 
    i ← i + 1
end for
repeat                                                        ▷ propagate smaller colors until convergence
    converged ← True
    for c ∈ Ω , l = 1, ..., L do
        if  $q_c^l \neq q_{\text{none}}$  &  $\alpha_c^l > 0$  then
            for c' ∈ Sc , l' = 1, ..., L do
                if  $q_{c'}^{l'} = q_c^l$  &  $\alpha_{c'}^{l'} > 0$  &  $\tilde{q}_{c'}^{l'} < \tilde{q}_c^l$  then
                     $\tilde{q}_c^l \leftarrow \tilde{q}_{c'}^{l'}$ 
                    converged ← False
                end if
            end for
        end if
    end for
until converged

```

Supplementary Figure 1 illustrates the algorithm on a case with one layer and three connected components.

Two-component incompressible flows

The model of two-component incompressible flows consists of Navier-Stokes equations for the mixture velocity \mathbf{u} and pressure p

$$\nabla \cdot \mathbf{u} = 0,$$

$$\rho \left(\frac{\partial \mathbf{u}}{\partial t} + (\mathbf{u} \cdot \nabla) \mathbf{u} \right) = -\nabla p + \nabla \cdot \mu (\nabla \mathbf{u} + \nabla \mathbf{u}^T) + \mathbf{f}_\sigma + \rho \mathbf{g}$$

and the advection equation for the volume fraction α

$$\frac{\partial \alpha}{\partial t} + (\mathbf{u} \cdot \nabla) \alpha = 0,$$

with the mixture density $\rho = (1 - \alpha)\rho_1 + \alpha\rho_2$, dynamic viscosity $\mu = (1 - \alpha)\mu_1 + \alpha\mu_2$, surface tension force $\mathbf{f}_\sigma = \sigma\kappa\nabla\alpha$ and gravitational acceleration \mathbf{g} , where σ is the surface tension and κ is the interface curvature. The mixture flow equations are discretized with the projection method [6], and the advection equation is solved using the procedure described in the Advection. The mixture density and viscosity fields are computed from the combined volume fraction field $\alpha = \min(1, \sum_q \alpha|_q)$. The surface tension force is computed by summation over all colors $\mathbf{f}^\sigma = \sum_q \sigma \kappa|_q \nabla \alpha|_q$ and the curvature $\kappa|_q$ is estimated from the volume fractions using the method of particles [23]. We apply a technique described in the Supplementary Methods to regularize the interface produced by the advection scheme which does not affect its asymptotic convergence or conservation properties but results in smoother surfaces at low resolutions. To simulate flows in complex geometries on a Cartesian mesh, we employ the method of embedded boundaries [10] which approximates the shape of the body with cut cells.

Code availability

The simulations are performed using the open-source solver Aphros available at <https://github.com/cselab/aphros>. The configuration files are located in https://github.com/cselab/aphros/tree/master/examples/205_multivof. An online demonstration of the method in two dimensions is at <https://cselab.github.io/aphros/wasm/hydro.html>.

References

- [1] ANNA, S. L. Droplets and bubbles in microfluidic devices. *Annual Review of Fluid Mechanics* 48, 1 (2016), 285–309.
- [2] ANNA, S. L., BONToux, N., AND STONE, H. A. Formation of dispersions using “flow focusing” in microchannels. *Applied physics letters* 82, 3 (2003), 364–366.

- [3] AULISA, E., MANSERVISI, S., SCARDOVELLI, R., AND ZALESKI, S. Interface reconstruction with least-squares fit and split advection in three-dimensional cartesian geometry. *Journal of Computational Physics* 225, 2 (2007), 2301–2319.
- [4] BALCÁZAR, N., LEHMKUHL, O., RIGOLA, J., AND OLIVA, A. A multiple marker level-set method for simulation of deformable fluid particles. *International Journal of Multiphase Flow* 74 (2015), 125–142.
- [5] BEATUS, T., TLUSTY, T., AND BAR-ZIV, R. Phonons in a one-dimensional microfluidic crystal. *Nature Physics* 2, 11 (2006), 743–748.
- [6] BELL, J. B., COLELLA, P., AND GLAZ, H. M. A second-order projection method for the incompressible navier-stokes equations. *Journal of Computational Physics* 85, 2 (1989), 257–283.
- [7] BRAKKE, K. A. The surface evolver. *Experimental mathematics* 1, 2 (1992), 141–165.
- [8] CANTAT, I., KERN, N., AND DELANNAY, R. Dissipation in foam flowing through narrow channels. *EPL (Europhysics Letters)* 65, 5 (2004), 726.
- [9] CHAN, D. Y., KLASEBOER, E., AND MANICA, R. Film drainage and coalescence between deformable drops and bubbles. *Soft Matter* 7, 6 (2011), 2235–2264.
- [10] COLELLA, P., GRAVES, D. T., KEEN, B. J., AND MODIANO, D. A cartesian grid embedded boundary method for hyperbolic conservation laws. *Journal of Computational Physics* 211, 1 (2006), 347–366.
- [11] COTTET, G.-H., AND MAITRE, E. A semi-implicit level set method for multiphase flows and fluid–structure interaction problems. *Journal of Computational Physics* 314 (2016), 80–92.
- [12] COYAJEE, E., AND BOERSMA, B. J. Numerical simulation of drop impact on a liquid–liquid interface with a multiple marker front-capturing method. *Journal of Computational Physics* 228, 12 (2009), 4444–4467.
- [13] CRAIG, V., NINHAM, B., AND PASHLEY, R. Effect of electrolytes on bubble coalescence. *Nature* 364, 6435 (1993), 317.
- [14] DEANE, G. B., AND STOKES, M. D. Scale dependence of bubble creation mechanisms in breaking waves. *Nature* 418, 6900 (2002), 839.
- [15] DEIKE, L., MELVILLE, W. K., AND POPINET, S. Air entrainment and bubble statistics in breaking waves. *Journal of Fluid Mechanics* 801 (2016), 91–129.
- [16] DEL CASTILLO, L. A., OHNISHI, S., AND HORN, R. G. Inhibition of bubble coalescence: Effects of salt concentration and speed of approach. *Journal of colloid and interface science* 356, 1 (2011), 316–324.
- [17] DOLLET, B., MARMOTTANT, P., AND GARBIN, V. Bubble dynamics in soft and biological matter. *Annual Review of Fluid Mechanics* 51, 1 (2019), 331–355.
- [18] FANG, J., RASQUIN, M., AND BOLOTNOV, I. A. Interface tracking simulations of bubbly flows in pwr relevant geometries. *Nuclear Engineering and Design* 312 (2017), 205–213.
- [19] GARRETT, C., LI, M., AND FARMER, D. The connection between bubble size spectra and energy dissipation rates in the upper ocean. *Journal of physical oceanography* 30, 9 (2000), 2163–2171.
- [20] GARSTECKI, P., STONE, H. A., AND WHITESIDES, G. M. Mechanism for flow-rate controlled breakup in confined geometries: A route to monodisperse emulsions. *Physical review letters* 94, 16 (2005), 164501.
- [21] HILL, C., AND EASTOE, J. Foams: From nature to industry. *Advances in Colloid and Interface Science* 247 (2017), 496–513. Dominique Langevin Festschrift: Four Decades Opening Gates in Colloid and Interface Science.
- [22] HIRT, C., AND NICHOLS, B. Volume of fluid (VOF) method for the dynamics of free boundaries. *Journal of Computational Physics* 39, 1 (1981), 201–225.
- [23] KARNAKOV, P., LITVINOV, S., AND KOUMOUTSAKOS, P. A hybrid particle volume-of-fluid method for curvature estimation in multiphase flows. *International Journal of Multiphase Flow* (2020), 103209.
- [24] KIGER, K. T., AND DUNCAN, J. H. Air-entrainment mechanisms in plunging jets and breaking waves. *Annual Review of Fluid Mechanics* 44 (2012), 563–596.
- [25] MARMOTTANT, P., AND RAVEN, J.-P. Microfluidics with foams. *Soft Matter* 5, 18 (2009), 3385–3388.

- [26] MATA, A., FLEISCHMAN, A. J., AND ROY, S. Characterization of polydimethylsiloxane (pdms) properties for biomedical micro/nanosystems. *Biomedical microdevices* 7, 4 (2005), 281–293.
- [27] MONTESSORI, A., TIRIBOCCHI, A., BONACCORSO, F., LAURICELLA, M., AND SUCCI, S. Lattice boltzmann simulations capture the multiscale physics of soft flowing crystals. *arXiv preprint arXiv:2003.11069* (2020).
- [28] PROSPERETTI, A. Vapor bubbles. *Annual Review of Fluid Mechanics* 49, 1 (2017), 221–248.
- [29] PROSPERETTI, A., AND TRYGGVASON, G. *Computational Methods for Multiphase Flow*. Cambridge University Press, Cambridge, UK, 2009.
- [30] RAVEN, J.-P., AND MARMOTTANT, P. Periodic microfluidic bubbling oscillator: Insight into the stability of two-phase microflows. *Physical review letters* 97, 15 (2006), 154501.
- [31] RAVEN, J.-P., AND MARMOTTANT, P. Microfluidic crystals: dynamic interplay between rearrangement waves and flow. *Physical review letters* 102, 8 (2009), 084501.
- [32] SAYE, R. I., AND SETHIAN, J. A. The voronoi implicit interface method for computing multiphase physics. *Proceedings of the National Academy of Sciences* 108, 49 (2011), 19498–19503.
- [33] SCARDOVELLI, R., AND ZALESKI, S. Analytical relations connecting linear interfaces and volume fractions in rectangular grids. *Journal of Computational Physics* 164, 1 (2000), 228–237.
- [34] STOFFEL, M., WAHL, S., LORENCEAU, E., HOEHLER, R., MERCIER, B., AND ANGELESCU, D. E. Bubble Production Mechanism in a Microfluidic Foam Generator. *Physical Review Letters* 108, 19 (MAY 7 2012).
- [35] STONE, H. A. Tuned-in flow control. *Nature Physics* 5, 3 (2009), 178–179.
- [36] TRYGGVASON, G., THOMAS, S., LU, J., AND ABOULHASANZADEH, B. Multiscale issues in DNS of multiphase flows. *Acta Mathematica Scientia* 30, 2 (2010), 551–562. Dedicated to professor James Glimm on the occasion of his 75th birthday.
- [37] VECCHIOLLA, D., GIRI, V., AND BISWAL, S. L. Bubble–bubble pinch-off in symmetric and asymmetric microfluidic expansion channels for ordered foam generation. *Soft matter* 14, 46 (2018), 9312–9325.
- [38] VELLA, D., AND MAHADEVAN, L. The “cheerios effect”. *American journal of physics* 73, 9 (2005), 817–825.
- [39] WEYMOUTH, G. D., AND YUE, D. K.-P. Conservative volume-of-fluid method for free-surface simulations on cartesian-grids. *Journal of Computational Physics* 229, 8 (2010), 2853–2865.
- [40] YOUNGS, D. L. Time-dependent multi-material flow with large fluid distortion. *Numerical methods for fluid dynamics* (1982).

Supplementary Movies

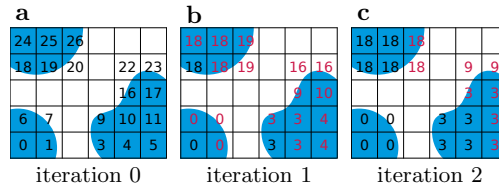
<https://polybox.ethz.ch/index.php/s/wtFIhSd77RG3Nyr>

- `s1_hex_one.mp4` — microfluidic crystal, hex-one
- `s2_hex_two.mp4` — microfluidic crystal, hex-two
- `s3_hex_three.mp4` — microfluidic crystal, hex-three
- `s4_hex_four.mp4` — microfluidic crystal, hex-four
- `s5_oscillator.mp4` — microfluidic crystal, oscillator
- `s6_bidisperse.mp4` — bidisperse foam
- `s7_clustering.mp4` — clustering of bubbles floating in water
- `s8_waterfall.mp4` — foaming waterfall

Supplementary Methods

Connected component labeling (Supplementary)

If the domain is decomposed into rectangular blocks for distributed parallelization, the algorithm is first applied to each block, then the halo cells are exchanged through communication and the whole procedure is repeated until global convergence. The total number of communication steps is the maximum length of a connected component divided by the block size. To reduce the number of communication steps, we use a heuristic for faster propagation of colors over the domain. The heuristic is executed before each iteration of the main algorithm. For each block, we consider only one corner cell (c, l) and its neighbors (c', l') and, if they are connected, collect the corresponding pairs of colors \tilde{q}_c^l and $\tilde{q}_{c'}^{l'}$ and transfer them all to one processor. Then we perform connected component labeling on this set of pairs and find a set of connected components. Finally, we broadcast them to other processors and replace each color with the minimal element of its connected component. With this heuristic, large connected components are identified after fewer iterations.



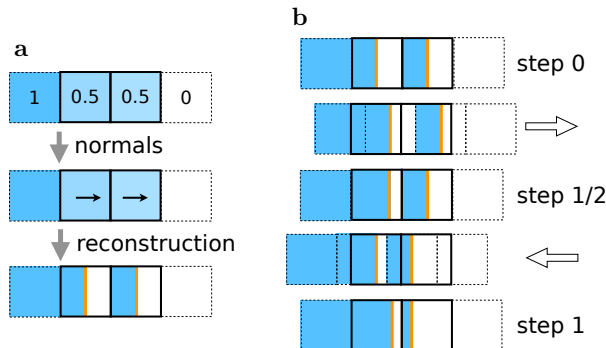
Supplementary Figure 1: Example of connected component labeling on a 6×5 grid with $L = 1$. Current colors \tilde{q}_c^l are shown with numbers. Initial colors (iteration 0) are indices enumerating all cells. Each iteration selects the minimal color over the 3×3 stencil. Colors updated at the current iteration are highlighted in red.

Interface regularization

Volume-of-fluid methods based on geometrical reconstruction, such as PLIC [3] employed in this work, offer good approximation properties, ensure boundness and conservation. They sharpen the interface of advected objects and hence reduce the numerical diffusion. However, the sharpening effect depends on the advection velocity. The choice of the frame of reference and the location of advected objects in a nonuniform velocity field affect the solution, which is undesirable. To mitigate this and also improve the accuracy at lower resolutions, we propose a technique for interface regularization based on PLIC. The idea is to apply forward and backward advection with a uniform velocity. This procedure is supposed to reduce the thickness of the interface and remove small spurious interface fragments. At the same time, it maintains volume conservation and boundness and does not affect the asymptotic convergence properties of the method.

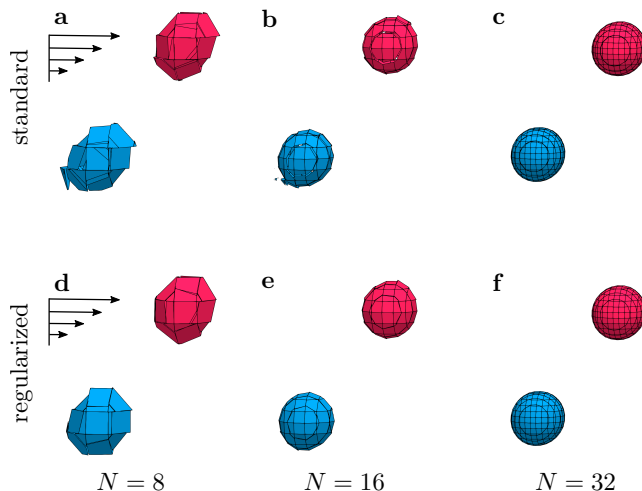
In one dimension, the procedure consists of two advection sweeps illustrated in Supplementary Figure 2. The initial interface (step 1) spans two cells with volume fractions $(0.5, 0.5)$. The forward step moves the interface to the right (step 1/2) and the volume fractions take values $(0.8, 0.5)$ as one cell fills with liquid from upstream. The backward step moves the interface to the left (step 1) reducing the volume fraction in the other cell, so they reach values $(0.8, 0.2)$. Note that after two steps, the field is again symmetric. In three dimensions, there are six advection sweeps with uniform velocities $\mathbf{u} = (U, 0, 0)$, $(-U, 0, 0)$, $(0, U, 0)$, $(0, -U, 0)$, $(0, 0, U)$, and $(0, 0, -U)$.

They are repeated after every time step of the simulation. The only parameter of the regularization is the advection velocity defined by the CFL number, which we set to $U\Delta t/h = 0.1$ for all simulations. To reduce the computational cost, the pairs of sweeps in each direction can be spread among every three consecutive time steps leaving only two sweeps per time step.



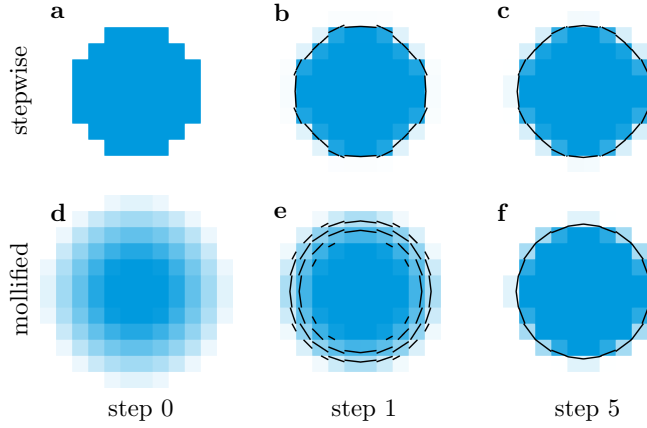
Supplementary Figure 2: (a) Stages of PLIC reconstruction in one dimension. The interface in each cell is replaced by a plane (orange) which is oriented by the estimated normal and cuts the cell at the given volume fraction. (b) Forward-backward advection reducing the interface thickness.

As noted above, the solution by the standard PLIC method depends on the choice of frame of reference. Moreover, at low resolutions the method can produce small spurious interface fragments. These effects are evident from the evolution of drops in a Couette flow shown in Supplementary Figure 3. The domain is a unit cube periodic in two directions and no-slip walls at the bottom and top with imposed velocities of 0 and 1 respectively. The mesh size is N^3 with $N = 8, 16$ or 32 . Initially, the drops are spheres of radius 0.15. The Reynolds number is $Re = \rho/\mu = 100$, the capillary number is $Ca = \mu/\sigma = 0.1$, and both components have the same density and viscosity. Since the flow is symmetric, in the exact solution the drops need to be symmetric as well. However, the numerical solution lacks this symmetry since the drops move at different speeds. Solving the problem with the standard method without regularization, we observe that the top (red) and bottom (blue) drops have different shapes and small interface fragments appear near the bottom drop at lower resolutions of $N = 8$ and 16 . Enabling the regularization not only removes the spurious fragments but also makes the shapes of the two drops more similar thus reducing their dependence on the frame of reference.



Supplementary Figure 3: Drops in Couette flow with the standard advection (a-c) and with interface regularization (d-f) on a mesh of N^3 cells. Snapshots at $t = 0.75$.

Another possible application of this technique is the regularization of initial conditions. Supplementary Figure 4 demonstrates two different fields representing a circle: a stepwise approximation and a mollified field. In both cases, a few steps of the regularization produce an interface with a thickness of one cell.



Supplementary Figure 4: Interface regularization applied to two fields representing a circle: stepwise (**a-c**) and radial piecewise linear (**d-f**).

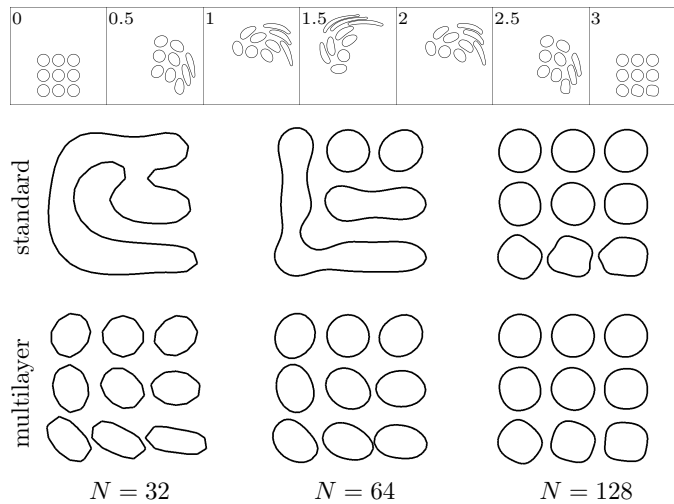
Supplementary Note: Verification

Time-reversed advection

The following setup is based on a classical test case for advection schemes. The initial volume fraction field describes nine circles and the velocity field defined in a two-dimensional unit domain represents a single vortex reversed at time $t = 1.5$

$$\mathbf{u}(x, y, t) = \begin{cases} (\sin \pi x \cos \pi y, -\cos \pi x \sin \pi y), & t < 1.5, \\ (-\sin \pi x \cos \pi y, \cos \pi x \sin \pi y), & t \geq 1.5. \end{cases} \quad (1)$$

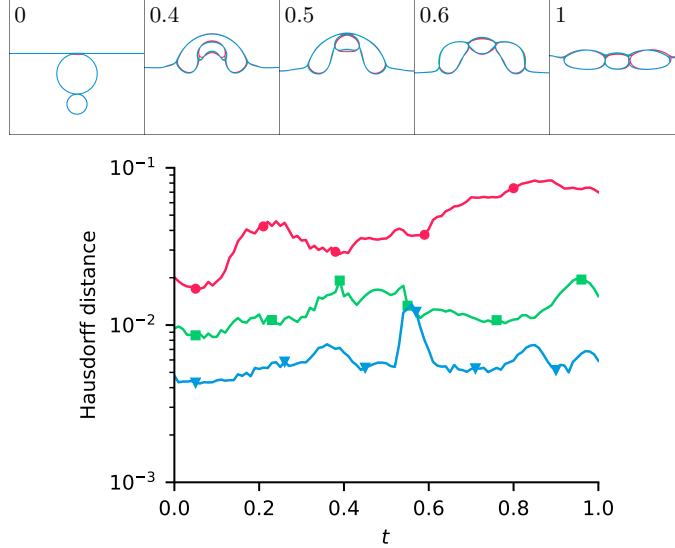
Since the advection equation is time-reversible, the exact solution at $t = 3$ coincides with the initial profile. Supplementary Figure 5 shows the solution in time and also compares the final profiles obtained by the standard PLIC advection and our multilayer method on a mesh of N^2 cells for $N = 32, 64$ and 128 . As seen from the final profiles at lower resolutions of $N = 32$ and 64 , the standard advection method merges some of the circles into larger objects. This effect is the origin of numerical coalescence. The deformations reduce that distances between the interfaces, and eventually they merge since the method cannot describe interfaces overlapping in the same cell. On the other hand, our multilayer advection method correctly maintains all circles separated. Both methods converge to the same solution with mesh refinement.



Supplementary Figure 5: Time-reversed advection of circles. Snapshots at times $t = 0, 0.5, 1, 1.5, 2, 2.5,$ and 3 (top) on the finest mesh of 64^2 cells with multilayer advection. Final profiles at $t = 3$ with standard advection (middle) and multilayer advection (bottom) on a sequence of meshes of N^2 cells with $N = 32, 64$ and 128 . The exact solution at $t = 3$ coincides with the initial profile.

Buoyancy-driven breakup

This case shows a buoyancy-driven breakup of two bubbles on a free surface and serves as a convergence test. The problem is solved in the unit domain $[0, 1]^2$ bounded by free-slip walls in the vertical direction and periodic in the horizontal direction. The mesh consists of N^2 cells for $N = 32, 64, 128,$ and 256 . The initial velocity is zero, and the volume fraction field represents a layer of gas $0.6 < y < 1$, one bubble of radius 0.15 and one bubble of radius 0.075. Parameters of the problem are the density $\rho_1 = 1$ and $\rho_2 = 0.01$, viscosity $\mu_1 = 0.01$ and $\mu_2 = 0.0001$, gravitational acceleration $g = 5$ and surface tension $\sigma = 0.01$. Supplementary Figure 6 presents the solution in time for various N and the corresponding Hausdorff distance between the interfaces computed on meshes with $(N/2)^2$ and N^2 cells. The bubbles rise and deform the free surface. The small bubble underneath penetrates the larger bubble and splits it into two equal parts. In the final configuration, three bubbles rest on the surface. The Hausdorff distance at $t = 0.4$ computed for $N = 64, 128$ and 256 amounts respectively to 0.0291, 0.0152 and 0.0067, which indicates a first order convergence rate.

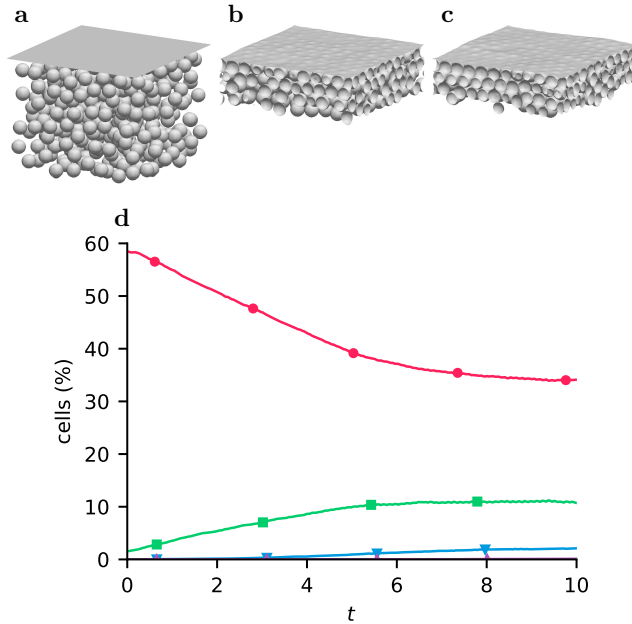


Supplementary Figure 6: Buoyancy-driven breakup of bubbles. Snapshots at $t = 0, 0.4, 0.5, 0.6,$ and 1 (top). Hausdorff distance between the interfaces computed on meshes with $(N/2)^2$ and N^2 cells (bottom). Lines correspond to $N = 64$ —●—, $N = 128$ —■—, and $N = 256$ —▲—.

Packing of rising bubbles

The case of close packing of rising bubbles demonstrates how overlapping interfaces are distributed over multiple layers. From this problem, we determine the number of layers L to use in other simulations and initially set it to $L = 8$. The problem is solved in the unit domain $[0, 1]^3$ on a mesh of 64^3 cells bounded by free-slip walls in the vertical direction and periodic in the other directions. The initial velocity is zero, and the volume fraction field represents a layer of gas $0.8 < y < 1$ together with 397 bubbles of radius 0.05 placed uniformly over the remaining volume. Parameters of the problem are the density $\rho_1 = 1$ and $\rho_2 = 0.01$, viscosity $\mu_1 = 0.01$ and $\mu_2 = 0.0001$, gravitational acceleration $g = 5$ and surface tension $\sigma = 0.1$.

Snapshots of the bubbles are shown in Supplementary Figure 7. The bubbles rise and closely pack creating bulges on the free surface. Supplementary Figure 7 shows the fraction of cells depending on the number of interfaces they contain. The initial separation between the bubbles is sufficiently large so that most cells contain only one interface. As the bubbles rise, the gaps between them reduce and fraction of cells with multiple interfaces increases. At the final time $t = 10$, the percentages of cells containing from one to six interfaces amount respectively to 34.11, 10.75, 2.13, 0.13, 0.0034, and 0.00076%. None of the cells contain more than six interfaces. Since the bubbles at the final time form a densely packed cluster and 99.9958% of cells contain four interfaces or less, we choose to use $L = 4$ layers for all other simulations.

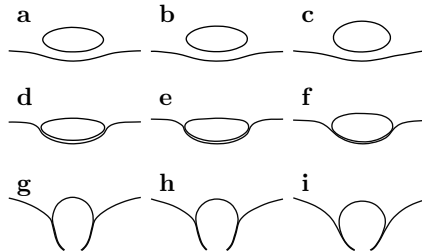


Supplementary Figure 7: Packing of rising bubbles. (a-c) Snapshots of the interfaces at $t = 0, 5$ and 10 . (d) Percentage of cells with one ●, two ■, three ▼, and four ▲ interfaces.

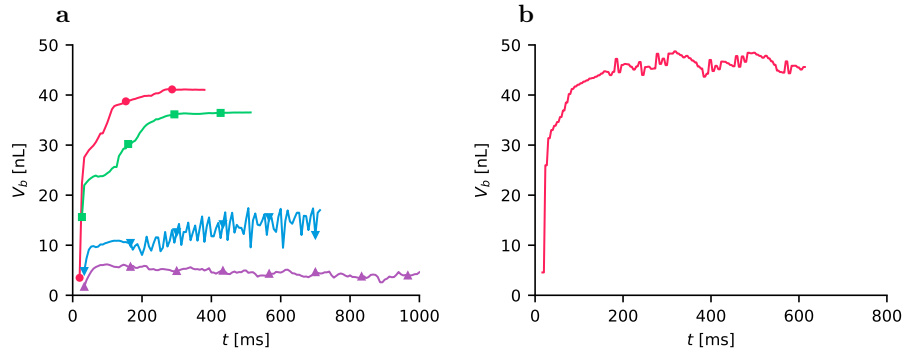
Drop impact on liquid-liquid interface

This test validates the model against experimental data on the gravity-driven impact of a liquid drop onto a liquid-liquid interface and shows that our method gives the same results as the multi-marked volume-of-fluid method [1]. The problem is solved in a rectangular domain of size $5 \times 10 \times 5$ cm on a mesh containing $160 \times 320 \times 160$ cells bounded by no-slip walls in the vertical direction and periodic conditions in the other directions. Parameters of the problem are taken from numerical study [1] based on experiment [2] (Combination 1): density $\rho_1 = 949$ and $\rho_2 = 1128$ kg/m³, viscosity $\mu_1 = 0.019$ and $\mu_2 = 0.0063$ Pa · s, gravitational acceleration $g = 9.8$ m/s² and surface tension coefficient $\sigma = 0.029$ N/m. They correspond to a water+glycerin drop falling in silicon oil. A spherical drop of a radius 5.1 mm is initially placed at a distance of 67 mm between its center and the interface.

Supplementary Figure 8 compares the slices of the interface obtained using the present method with numerical data [1] and experimental data [2]. Then the liquid film between the liquids drains but no coalescence occurs. The falling drop approaches the surface separating the liquids, creates a bulge and eventually rests on the surface. Our algorithm produces the same results as method [1] and both agree with the experimental data.



Supplementary Figure 8: Drop impact on liquid-liquid interface. Central slices at $t = 0.63, 0.67,$ and 0.77 s produced by the present method (a,d,g) compared to images from numerical study [1] (b,e,h) and experimental data [2] (c,f,i).



Supplementary Figure 9: Microfluidic crystals. Evolution of the volume of generated bubbles. (a) Stationary crystalline structures in channel of length $L = 6.8$ mm. Hex-one ($P_g = 216$ Pa) —●—, hex-two ($P_g = 194$ Pa) —■—, hex-three ($P_g = 149$ Pa) —▲—, and hex-four ($P_g = 140$ Pa) —◆—. (b) Spontaneous transitions between hex-one and hex-two at $P_g = 225$ Pa and the channel length $L = 5.3$ mm.

density of liquid	ρ_l	1000	kg / m ³
density of gas	ρ_g	100	kg / m ³
viscosity of liquid	μ_l	0.25	mPa · s
viscosity of gas	μ_g	0.025	mPa · s
surface tension	σ	3.6	mN / m
liquid flow rate	Q_l	0.3	mL / h
bubble breakup period	T_b	$0.5 W_0^2 H / Q_l$	
device height	H	100	μm
orifice width	W_0	110	μm
collection channel width	W	1000	μm
collection channel length	L	6800	μm
computational cell size	h	10.1	μm
Case of bubbling oscillator:			
collection channel length	L	5300	μm
bubble breakup period	T_b	$0.46 W_0^2 H / Q_l$	
inlet pressure	P_g	225	Pa

Supplementary Table 1: Microfluidic crystals. Simulation parameters.

density of liquid	ρ_l	1021	kg / m ³
density of gas	ρ_g	41	kg / m ³
viscosity of liquid	μ_l	1.25	mPa · s
viscosity of gas	μ_g	0.05	mPa · s
surface tension	σ	35.2	mN / m
bubble generation period	T	111	μs
volume of generated bubble	V_b	0.68	nL
gas volume fraction	Φ	0.645	—
inlet mean velocity	v_{mean}	2.09	m / s
inlet flow rate	Q	12	mL / h
channel height	H	60	μm
inlet channel width	W_0	75	μm
inlet channel length	L_0	816	μm
collection channel width	W	1600	μm
collection channel length	L	1600	μm
computational cell size	h	2.51	μm

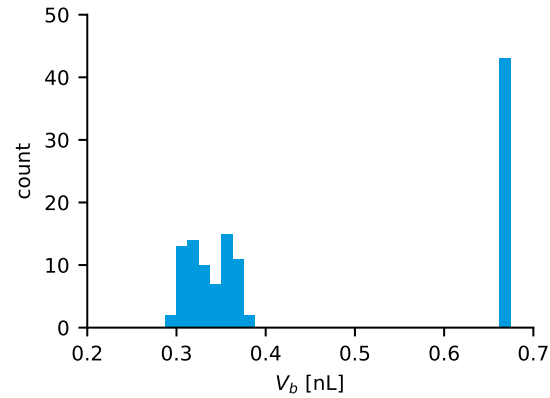
Supplementary Table 2: Bidisperse foam generation. Simulation parameters.

density of liquid	1000	kg / m ³
density of gas	30	kg / m ³
viscosity of liquid	$2 \cdot 10^{-3}$	Pa · s
viscosity of gas	$2 \cdot 10^{-5}$	Pa · s
surface tension	18	mN / m
bubble diameter	2	mm
domain length	30	mm
domain width	30	mm
domain height	20	mm
computational cell size	0.16	mm

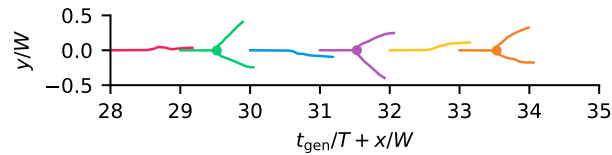
Supplementary Table 3: Clustering of bubbles. Simulation parameters.

density of liquid	1000	kg / m ³
density of gas	10	kg / m ³
viscosity of liquid	10^{-3}	Pa · s
viscosity of gas	10^{-5}	Pa · s
surface tension	72	mN / m
waterfall mean velocity	1.5	m/s
waterfall thickness	5	mm
domain length	200	mm
domain width	100	mm
domain height	100	mm

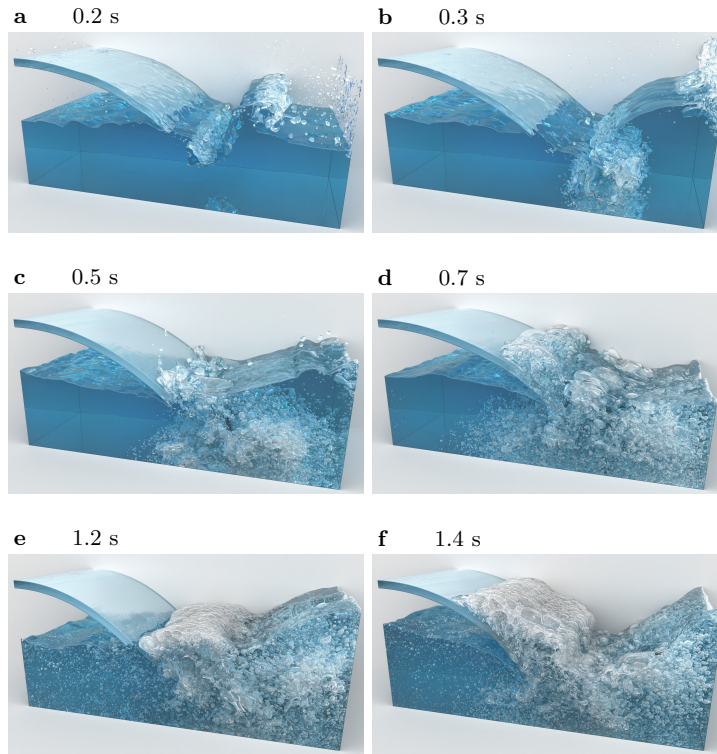
Supplementary Table 4: Foaming waterfall. Simulation parameters.



Supplementary Figure 10: Bidisperse foam generation. Histogram of the bubble volume after 80 cycles.



Supplementary Figure 11: Bidisperse foam generation. Trajectories of the centroids of bubbles generated at $t_{\text{gen}}/T \in [28, 34]$ shifted along the horizontal axis by the generation time. Coordinates of the centroid x and y are relative to the generation point.



Supplementary Figure 12: Foaming waterfall. Snapshots of the interface at $t = 0.2$ (a), 0.3 (b), 0.5 (c), 0.7 (d), 1.2 (e), and 1.4 s (f).

References

- [1] COYAJEE, E., AND BOERSMA, B. J. Numerical simulation of drop impact on a liquid–liquid interface with a multiple marker front-capturing method. *Journal of Computational Physics* *228*, 12 (2009), 4444–4467.
- [2] MOHAMED-KASSIM, Z., AND LONGMIRE, E. K. Drop impact on a liquid–liquid interface. *Physics of Fluids* *15*, 11 (2003), 3263–3273.
- [3] YOUNGS, D. L. Time-dependent multi-material flow with large fluid distortion. *Numerical methods for fluid dynamics* (1982).